In situ visualization of chemical interdiffusion phenomena in ultrathin graphene intercalated Co/Pt heterostructures for spintronics

Alejandra Guedeja-Marrón [1,2] Fernando Ajejas [3] Adrián Gudin [3,4] Icíar Arnay [3] Lucas Perez [1,3] Paolo Perna [3] and Maria Varela [1,2,*]

[1]*Departamento de Física de Materiales, Universidad Complutense de Madrid, 28040 Madrid, Spain*
[2]*Instituto Pluridisciplinar, Universidad Complutense de Madrid, 28040 Madrid, Spain*
[3]*IMDEA Nanoscience, C/ Faraday 9, Campus de Cantoblanco, 28049 Madrid, Spain*
[4]*Departamento de Física de la Materia Condensada & Condensed Matter Physics Center (IFIMAC), Universidad Autónoma de Madrid, Campus de Cantoblanco, 28049 Madrid, Spain*

(Received 16 February 2025; revised 22 April 2025; accepted 23 April 2025; published 24 June 2025)

Graphene-based magnetic epitaxial heterostructures, where an ultrathin layer of a ferromagnetic metal is sandwiched between a heavy metal and a graphene monolayer, have been widely studied due to their easily tunable interfacial driven spin-orbit interactions. The interplay between orbital hybridization and symmetry breaking at the interfaces in systems like graphene/Co grown epitaxially on Pt results in enhanced perpendicular magnetic anisotropy and sizeable antisymmetric exchange interaction, enabling the possibility to stabilize thermally stable chiral spin textures and their manipulation with external stimuli. However, in order to properly exploit the functionality of such heterostructures, the crystal structure, composition, and integrity of the ultrathin ferromagnetic metallic layer must be understood down to the atomic level. For this aim, the characterization of thermally activated atomic processes taking place during growth, along with changes likely taking place during future device performance derived from Joule heating, is a must. In this work, we use *in situ* atomic resolution electron microscopy and spectroscopy techniques to investigate thermally activated interdiffusion phenomena at Co/Pt interfaces in the range of 300–773 K. We show how significant alloying takes place at the Co/Pt interface for higher annealing temperatures. Such interdiffusion affects the magnetic properties of the layers, enhancing the layer coercivity. Such direct visualization of the thermally induced interdiffusion effects offers a pathway for optimizing graphene-based magnetic epitaxial systems for robust device integration.

DOI: 10.1103/PhysRevMaterials.9.064411

I. INTRODUCTION

The past few decades have witnessed the birth of new fields, such as spin-transport electronics or spintronics, and, more recently, spin-orbitronics [1,2], arising from the pivotal role that the electronic orbital moment plays in magnetic properties [3]. Much of the physics behind the emergence of these fields results from the interactions between spin and angular momentum at the atomic level ruled by spin-orbit coupling (SOC). Materials that exhibit high SOC are potential candidates for converting charge currents to large spin-currents, thus they have attracted a lot of interest in the scientific community for their potential use in a novel generation of low-power spintronic devices [4,5]. For instance, heterostructures where a thin ferromagnetic (FM) layer is sandwiched in between a heavy metal (HM) and a two-dimensional (2D) material constitute an interesting playground in which to explore nontrivial physical spin-related and interface-driven phenomena effects [5–11]. Long-range magnetic order along with spin filtering has been achieved in graphene (Gr) [6,12], as well as the introduction of giant SOC [13]. As a result, Gr-based heterostructures can be engineered to tailor interfacial SOC. In fact, it has been shown that the interplay between orbital hybridization and symmetry breaking at Gr/FM/HM interfaces such as Gr/Co grown epitaxially on heavy metals, such as Pt or Ir, results in a strong anisotropy of the Co orbital moment, proximitized in the Gr π band, along with a non-negligible mismatch in the surface potentials of the layers. These features result in enhanced perpendicular magnetic anisotropy (PMA) along with sizeable antisymmetric exchange interaction [14], making it possible to stabilize thermally stable chiral spin textures and their manipulation with electric fields.

However, harnessing these factors relies on producing heterostructures with high-quality interfaces that can promote adequate electronic coupling, since the macroscopic behavior will be largely affected not just by dimensionality effects but also by the local crystal structure, composition, and type of atomic bonding at the interface between constituent materials. For example, the crystal structure of ultrathin Co layers in Gr/Co/Pt heterostructures has been found to differ from the hexagonal (HCP) bulk structure in that it is stabilized into a face-centered-cubic (FCC) phase, manifesting an

*Contact author: mvarela@ucm.es

enhanced PMA and a sizeable Dzyaloshinskii-Moriya interaction [14,15], with Rashba character in the low thickness limit [16]. In this scenario, the crystal structure, composition, and integrity of the ultrathin FM layer in Gr/FM/HM heterostructures, just two or three monolayers thick, must be examined and understood at the atomic level, including control of interfacial parameters such as physical or chemical roughness. Such studies must be carried out under conditions other than room temperature (e.g., at higher T values) in order to understand growth mechanisms or also phenomena that may take place during future device operation subject to heating. For example, any device with functionalities driven by electrical currents may be subject to Joule heating, which may significantly increase the local temperature. Thermal energy transferred into the system may give rise to changes at interfaces that could modify functionality and jeopardize performance. This could be the case, e.g., if heating were to promote disorder in the form of step disorder or activate chemical interdiffusion phenomena in Gr/FM/HM heterostructures.

Fundamental studies that can characterize such systems with atomic resolution in real space hold the key to understanding such processes. To study the effects of heating, *ex situ* experiments are traditionally carried out by comparing the materials before and after controlled annealing processes. Though interesting, these procedures lack information on intermediate phenomena since only data from the initial and final states are recorded [17]. On the other hand, *in situ* heating tests provide a good approach for real-time observation of these thermally activated processes. In this work, we address the visualization of chemical interdiffusion in Co/Pt interfaces when just a few monolayers of magnetic species are present. For this aim, high-quality epitaxial Gr/Co/Pt heterostructures, where a 2–3 monolayers (ML) thick FM Co layer is sandwiched between an epitaxial Pt(111) buffer and a Gr layer, have been successfully grown on insulating oxide single-crystal substrates such as MgO, $SrTiO_3$, (STO) or sapphire [9,14,15]. Previous works have suggested the activation of chemical intermixing in epitaxial Co/Pt interfaces grown underneath graphene monolayer [18], using surface-sensitive techniques. Here, we use aberration corrected scanning transmission electron microscopy (STEM) combined with electron energy-loss spectroscopy (EELS) techniques to study *in situ* the effects of heating in Gr/Co/Pt(111) heterostructures where the Co layer is barely 1 nm thick, with a special focus on any Co/Pt intermixing and the formation of any other phases. These techniques combine atomic resolution with single-atom sensitivity both in imaging and spectroscopy modes, and they are compatible with the use of specimen holders capable of heating the materials in a controlled fashion while maintaining atomic resolution. Our results should help to understand growth processes at high temperatures, and also to prevent undesired effects during operation of future devices based on building blocks such as this type of Gr/FM/HM stacking.

II. METHODS

A. Sample preparation

Gr-based epitaxial multilayers were grown in ultrahigh-vacuum (UHV) conditions on commercially available (111)-oriented oxide single crystals STO and MgO in a multipurpose UHV system combining molecular beam epitaxy (MBE), direct current and radiofrequency sputtering (dc-rf sputtering), chemical vapor deposition (CVD), and x-ray photoelectron spectroscopy, ultraviolet photoelectron spectroscopy, and low-energy electron diffraction (XPS-UPS-LEED) connected chambers. An epitaxial (111)-oriented Pt buffer with nominal thicknesses of 50 nm was deposited by dc sputtering in 8×10^{-1} Pa Ar partial pressure at 670 K with a deposition rate of 0.3 Å/s. Subsequently, the Pt/STO(111) template was annealed at 1025 K in UHV (1×10^{-7} Pa) before the insertion of ethylene gas through a leak valve with a partial pressure of 2×10^{-6} Pa for 30 min to grow Gr on top of Pt. Then, the sample was cooled down to room temperature (RT). Co was hence deposited on the top of Gr/Pt/STO(111) by e-beam evaporation at RT with a deposition rate of 0.04 Å/s until a nominal thickness of 1 nm. The further Co intercalation below Gr was promoted by thermal annealing at 550 K [18]. This procedure leads to the formation of a homogeneous Co layer with high structural order and sharp interfaces. Finally, a 5 nm capping Ta layer was dc sputtered at RT for passivation purposes to protect the Gr layer when exposed to air. The grown epitaxial Gr/Co/HM (111) oriented heterostructures are expected to present large PMA even for very thin Co layers [15].

B. Electron microscopy

Atomic resolution STEM-EELS measurements were obtained using an aberration corrected ARM200cF JEOL electron microscope equipped with a Gatan Quantum EEL spectrometer. For *in situ* heating studies, a DENSsolutions Lightning D9+ double tilt holder was employed. Cross-section samples were prepared by focused ion beam (FIB) and deposited on specific microelectronic mechanical system (MEMS) chips for these measurements. Principal component analysis (PCA) [19] was used for denoising the EELS data when necessary. EELS compositional maps were produced by conventional procedures such as integration of the EELS signal after background subtraction using a power-law fit.

C. X-ray diffraction

Structural characterization of Gr/Co/Pt stacks by x-ray diffraction (XRD) was performed using a commercial Rigaku SmartLab SE multipurpose x-ray diffractometer, equipped with a nonmonochromatic Cu $K\alpha$ source ($\lambda = 1.54$ Å) in a parallel beam geometry. Additionally, a Ge $(220) \times 2$ monochromator was used to perform θ-2θ measurements at a high angle. X-ray reflectivity (XRR) measurements and electron density profiles were simulated using the REFLEX software [20], using the Nelder-Mead simplex algorithm. Density values were fixed at bulk values for both Pt ($\rho = 21.5\ \mathrm{g/cm^3}$) and Co ($\rho = 8.9\ \mathrm{g/cm^3}$).

D. Magnetic characterization

The magnetic-field-dependent magnetization curves of the structures have been investigated by Kerr magnetometry (MOKE) at room temperature [21,22]. The samples were placed in a stepper-motorized eucentric goniometer head that

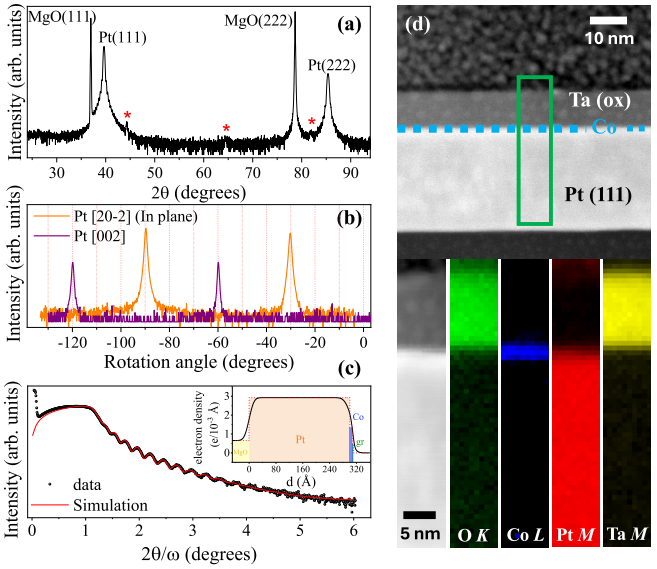

FIG. 1. (a) X-ray θ-2θ out-of-plane diffraction patterns showing that the Pt [111] and [222] crystallographic reflections are coherent with the MgO [111] substrate. The red stars indicate the reflections caused by the crystallized Ag paint used to attach the substrate to the UHV chamber's sample holder. (b) Rotation scans around Pt [20-2] and Pt[002] reflections showing sixfold symmetry. (c) Reflectometry measurement (data points) and data simulation (red solid line) on Gr/Co(1)/Pt(30) stacks deposited on MgO[111] [9,15]. The inset shows the electron density profile used as a function of depth within the heterostructure. Different blocks corresponding to the substrate (MgO), Pt, Co, and graphene (gr) layers have been highlighted in yellow, orange, blue, and green, respectively. (d) Right: HAADF-STEM image of the Pt/Co/Gr heterostructure, with a green rectangle highlighting the region where an EEL spectrum image was acquired. The adjacent panels, from left to right, represent the simultaneously acquired HAADF signal along with compositional maps showing the integrated EELS extracted from the O K (green), Co $L_{2,3}$ (blue), Pt $M_{4,5}$ (red), and Ta $M_{4,5}$ (yellow) edges.

keeps the reflection plane fixed, and out-of-plane vectorial resolved hysteresis loops have been acquired under an external magnetic field applied along the normal to surface direction. The measurements have been done in polar geometry, hence the out-of-plane component of the magnetization has been acquired.

III. RESULTS

The structural quality of the samples, averaged over long lateral distances, was probed by XRD. Figures 1(a) and 1(b) illustrate XRD measurements from a Gr/Co(1 nm)/Pt(30 nm)/MgO[111] heterostructure. The out-of-plane θ-2θ scan [Fig. 1(a)] shows crystallographic reflections from both the substrate and the buffer layer, corroborating a coherent, (111)-oriented growth of Pt on the substrate. The rotation scans around Pt[202] ($2\theta_{202} = 67.82°$) and Pt[200] ($2\theta_{200} = 46.34°$) reflections [Fig. 1(b)] confirm fully epitaxial growth of the Pt buffer on MgO[111]. The measured sixfold symmetry at the Pt[200] reflection, instead of the expected threefold symmetry, indicates the presence of two equivalent twin-boundary domains. Figure 1(c) shows a low-angle reflectivity measurement in the Gr/Co/Pt stack. The presence of Kiessig fringes at low angles, as well as the observation of these oscillations even at high angles [Fig. 1(a)], points to low roughness and flatness of the interfaces on a long lateral lengthscale, confirming that interfaces are atomically flat over long lateral distances. The refinement of the reflectivity (continuous line) shows good agreement with nominal thickness for both Pt and Co layers. The inset shows the electron density profile as a function of depth within the heterostructure. Different blocks corresponding to the substrate (MgO), Pt, Co, and graphene (gr) layers have been highlighted in yellow, orange, blue, and green, respectively. Graphene was modeled as a carbon layer of 0.345 nm and fixed in the simulation; only the thicknesses and roughness of the Pt and Co layer were allowed to vary during the fitting, yielding values of $t_{Pt} = 30.0$ with a roughness of 1.4 nm, and $t_{Co} = 0.73$ nm with a roughness of 0.5 nm. Data from similar samples grown on STO have been reported in previous works and exhibit similar features, confirming the high-quality crystal structure of the heterostructures [7,9,14,15].

Real-space compositional maps also point to sharp, well-defined layers. Figure 1(d) displays several compositional maps obtained from EEL spectrum images, corresponding to the O, Co, Pt, and Ta species from a Gr/Co(1 nm)/Pt(30 nm) heterostructure capped with Ta oxide to prevent surface degradation. Nominal thicknesses are shown in parentheses. The green rectangle on the high-angle annular dark field (HAADF) image on the left highlights the region where the EEL spectrum image was acquired. The O K, Co $L_{2,3}$, Ta $M_{4,5}$, and Pt $M_{4,5}$ EELS edges with onsets near 528, 779, 1735, and 2122 eV [23], respectively, were analyzed to produce the compositional maps in the lower panels. Both the Co layer and the Co/HM interface appear flat. The Gr layer on top of the FM acts as a barrier for O diffusion, preventing major oxidation of the Co. This finding is deduced from the observation of the O K map (green), which shows no noticeable O signal in the Co layer. Thus, we can conclude that the Gr/Co is successfully passivated with the Ta-oxide capping, and the Co layer remains unoxidized. Previous findings reported for similar samples [7,9,14,15] confirm the correct intercalation of the FM Co layer during the synthesis procedure. These results give further proof of the good chemical integrity of the as-grown layers.

The samples are fully ferromagnetic at room temperature, even if the FM layer is only a few monolayers thick. However, using increased temperatures for the Gr intercalation process clearly affects their magnetic properties. Figure 2 represents the magnetic characterization of two epitaxial Gr/Co(1 nm)/Pt(111) heterostructures, in the form of vectorial resolved MOKE magnetohysteresis (MH) loops. The blue dots correspond to a Gr/Co(1 nm)/Pt sample where Co intercalation was performed reaching a maximum temperature of 550 K. The red data, on the other hand, correspond to the hysteresis loop of a Gr/Co(1 nm)/Pt(111) heterostructure where the maximum annealing temperature during the intercalation process was 675 K. These results point to a very relevant effect of the intercalation temperature on the heterostructure magnetic properties. In fact, previous studies carried out by macroscopically averaged surface-sensitive techniques, such

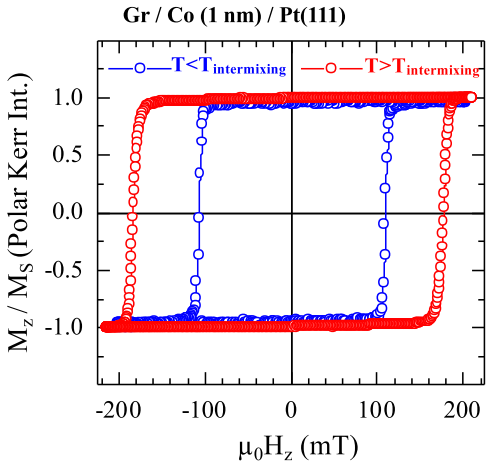

FIG. 2. Vectorial resolved MOKE MH loops normalized to the saturation magnetization M_S of epitaxial Gr/Co(1 nm)/Pt(111), measured at RT. Blue dots refer to the sample where the Co intercalation process was carried out reaching the maximum temperature of 550 K ($T < T_{\text{intermixing}}$). Data depicted with red dots correspond to a heterostructure where the Co intercalation was carried out reaching the maximum temperature of 675 K ($T > T_{\text{intermixing}}$). The higher temperature provokes an enhancement of the coercive field, suggesting an enhancement of magnetic anisotropy while preserving the sharp and abrupt magnetization reversal pathways.

as XPS, suggest that chemical intermixing between Co and Pt may take place at temperatures above 595 K [18], a value that we will define as $T_{\text{intermixing}}$ from now on. These studies demonstrate that the magnetic properties of the sample treated at 675 K (red data) are affected by the higher temperature applied, giving a first hint that temperature-induced effects are relevant. While both hysteresis loops present a square shape with sharp transitions in the reversal processes, the sample treated at a temperature $T > T_{\text{intermixing}}$ (red open points) shows a larger coercivity of 180 mT compared to the 110 mT of the heterostructure treated at $T < T_{\text{intermixing}}$ (blue open points). A preliminary explanation for this behavior is based on a possible Co-Pt intermixing induced by temperature, as suggested by previous reports. Perhaps the larger magnetic anisotropy manifested by the Co-Pt alloy that originated from larger SOC within the FCC structure, which is related to the anisotropy of the orbital magnetic moment, could result in such enhanced coercivity [15]. However, further proof of the microscopic structure of these interfaces is needed.

To probe any locally induced Co-Pt intermixing, annealing *in situ* experiments were conducted on samples where Co had been intercalated at temperatures $T < T_{\text{intermixing}}$ to study any potential effects of temperature on the structure of the layers and interfaces. The combination of *in situ* heating experiments with aberration corrected STEM provides optimal vacuum conditions, high spatial resolution capabilities for real-time observation, and EELS compositional analysis. *In situ* annealing experiments here were carried out using heating (Wildfire) nanochips from DENSsolutions [see Fig. 3(a)]. These chips provide uniform temperature distribution across the sample area, crucial for consistent experimental conditions. They allow for reaching temperatures up to 1573 K, within 200 degrees per millisecond and negligible bulging of the SiN_x

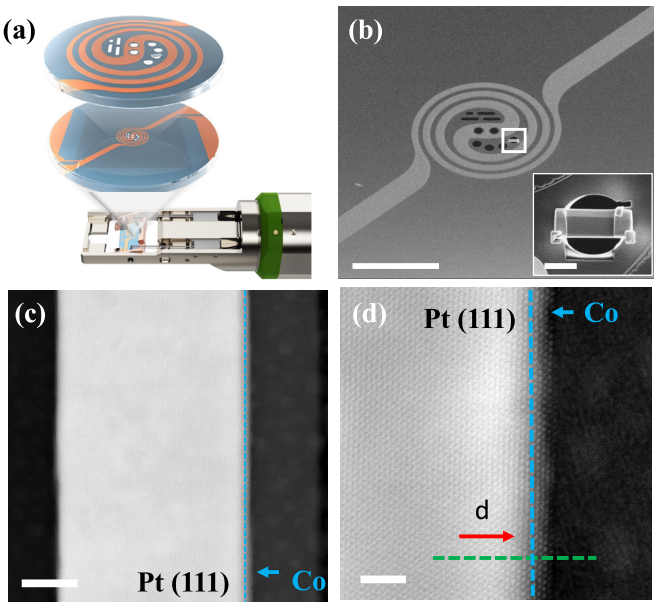

FIG. 3. (a) Wildfire nanochip illustration. The metal spiral is represented in orange and the silicon nitride membrane in blue. Adapted from Ref. [25]. (b) Low magnification SEM image of the *in situ* heating Wildfire nanochip with a transferred lamella prepared by FIB-SEM. The inset shows a high magnification of the milled lamella deposited on a through-hole for STEM observation. Scalebars correspond to 100 μm in the low mag image, and 5 μm for the image in the inset. (c) HAADF-STEM low magnification image of a Gr/Co/Pt(111) sample grown on a STO substrate (with 2–3 Co MLs and $t_{\text{Pt}} = 30$ nm), and capped with Ta oxide. The ultrathin Co layer is marked with the blue arrow, and the Co/Pt interface is marked with a blue dashed line. Some surface contamination is observed. (d) Atomic resolution HAADF image of the Pt/Co interface. A green line indicates the region where EELS linescans were acquired during the *in situ* heating experiment. The scale bar of the low magnification STEM image (c) is 10 nm, whereas in the high magnification ADF image (d) it represents 2 nm.

support membranes up to 773 K [24]. Therefore, they provide reliable support for atomic resolution observation while heating without defocusing or spatial drift: the region of interest remains in the field of view during the annealing process with high sample stability. These Wildfire nanochips present a four-contact configuration connected to a microheater to control and determine the precise temperature of the sample [see Figs. 3(a) and 3(b)].

A cross-sectional specimen consisting of a lamella of a TaOx/Gr/Co/Pt/STO(111) heterostructure was mounted on such a MEMS nanochip, as shown in Fig. 3(b). STO is preferred over MgO for focused ion beam (FIB) lamella preparation due to a higher electric conductivity, which reduces charging effects during milling. This nanochip setup allows stable, atomic-resolution imaging of the specimens at room and high temperature. Figures 3(c) and 3(d) show cross-section HAADF images at RT of the Gr/Co (1 nm)/Pt heterostructure mounted on the heating chip. The ultrathin Co layer is marked with blue arrows in both images. The Co/Pt interface is epitaxial and coherent, and the ultrathin Co layer is continuous over long lateral distances in good agreement with

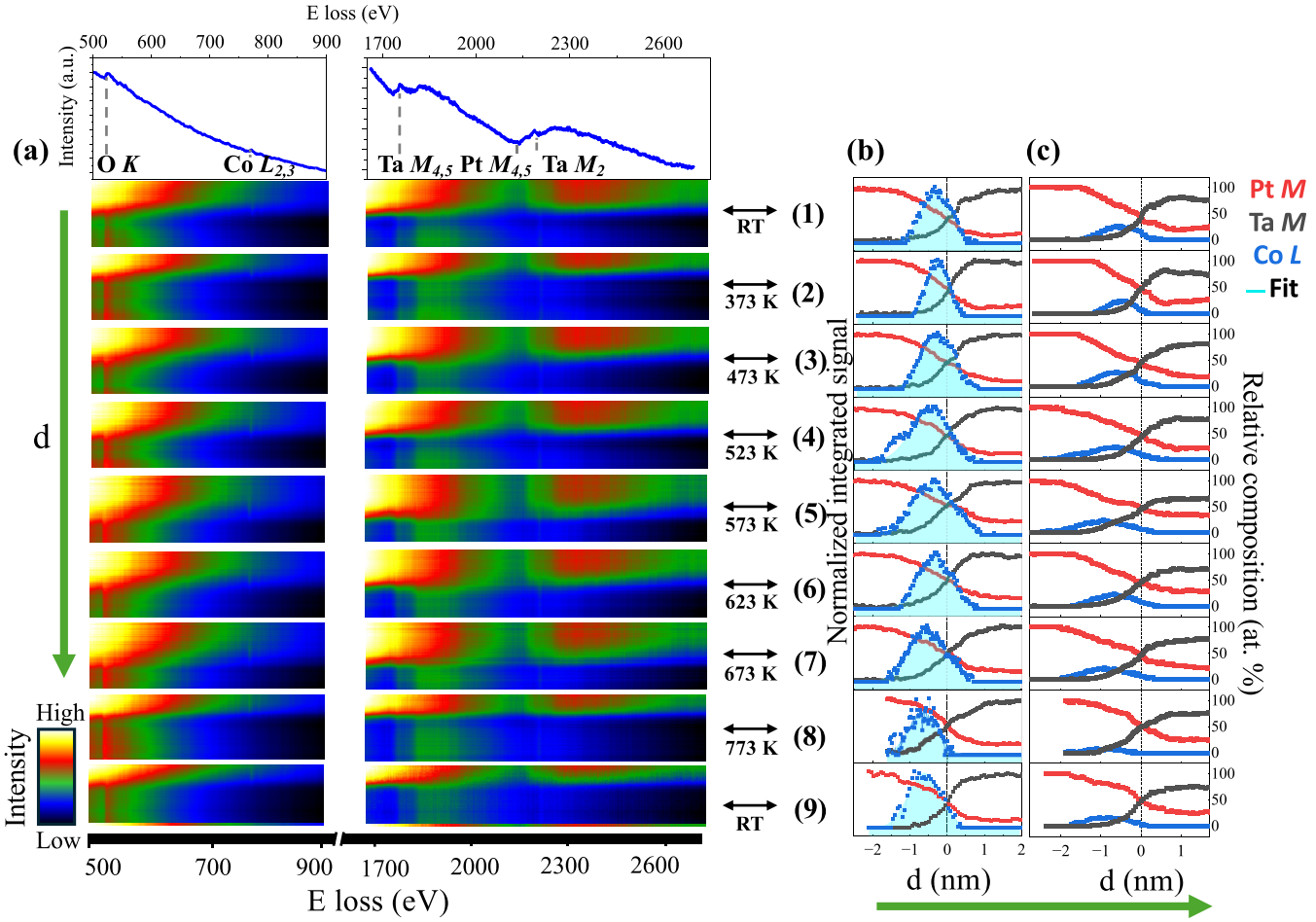

FIG. 4. (a) Top: Averaged EEL spectrum, in arbitrary units, showing all edges of interest for the sake of clarity. Then, from the second panel top to bottom: EELS linescans obtained at room temperature and 373, 473, 523, 573, 623, 673, and 773 K and then again at room temperature after quenching at the very bottom. The horizontal scale represents the energy loss, while the vertical direction, marked with a green arrow, corresponds to the position of the electron beam along the scan direction, marked with a green line in Fig. 3(d). Thus, every horizontal line corresponds to the EEL spectrum measured at that precise position, and so on. The EELS signal intensity is depicted in a false color scale. PCA was applied to remove random noise. (b) Normalized integrated signals for the Co (blue), Pt (red), and Ta (black) signals across the Ta/Gr/Co/Pt(111) stack. Gaussian fits to the Co signal profiles are shown in solid cyan. (c) Relative composition, in atomic percent, for Co (blue), Pt (red), and Ta (black), calculated for all linescans on a matching order from top to bottom. A green arrow marks the direction of the scan, as in (a). The center of mass of the Co layer shifts towards the Pt layer as the Pt and Co relative compositions drop within the Co thickness range, showing the presence of thermally activated significant chemical intermixing for annealing temperatures of 523 K and above.

XRR data. Some occasional steps, one atomic plane high, are observed at both the Pt/Co interface and on the Co surface. The Ta oxide capping layer is also homogeneous.

The green line shown in Fig. 3(d) marks the region where the EELS linescans across the Co/Pt interface shown in Fig. 4 were acquired by scanning the electron beam along the line while acquiring EEL spectra. *In situ* heating experiments were carried out by annealing the sample from room temperature all the way up to 773 K (500 °C). During this process, EEL profiles were measured at RT and 373, 473, 523, 573, 623, 673, and 773 K. During the process, the temperature was held constant at each step value for approximately 10 min to allow for stabilization before acquiring the EELS data. After spectroscopic data acquisition, the temperature was increased to the next value listed above. Only after the final annealing process at 773 K was the sample quenched back to RT. All resulting EELS linescans are shown in Fig. 4, with an average EEL spectrum on top showing where all the edges of interest are visible. Below, all linescan data are plotted, ordered from the lowest (RT, top) to the higher temperature values (towards the bottom panel). The dataset measured after quenching back to room temperature is shown at the very bottom end of the panel. For each panel, the horizontal axis plots the energy loss, while the vertical axis represents the position of the spectrum along the line. The color map represents the spectral intensity in a false color scale. All spectra are displayed on a matching energy scale.

Figure 4(b) depicts the normalized integrated EEL signals extracted from the corresponding panels in Fig. 4(a), side to side. Signals shown correspond to the Co $L_{2,3}$ (blue), Pt $M_{4,5}$ (red), and Ta $M_{4,5}$ (black) edges as a function of distance across the scan [green arrow in Fig. 3(a)]. The C *K* signal was not measured here, so no C mapping is presented, although the integrity of the Gr layer has been shown in a previous

work [14]. The signals were quantified for every spectrum by integrating the edge signal after background subtraction using a power-law fit. The positions of the Pt, Co, and Ta layers can be easily identified via inspection of these profiles, all of them being well defined. For visual clarity, the origin of the x-axis has been set at the crossover between the Pt and Ta signals. It is worth noting that the interface profiles may not appear completely sharp, but this effect is due to beam-broadening effects associated with channeling. The relative sample thickness was evaluated using the log-ratio (relative) method [26] with *Digital Micrograph* routines and found in the order of 29.9 ± 4.4 nm on average. The error has been calculated from the standard deviation of the data. For such thickness values, a significant channeling is to be expected for these heavy elements, so the apparent interface width observed in these profiles represents an upper estimate for the actual interface chemical width. It is also worth noting that the Pt signal profiles appear to exhibit a significant tail extending into the Ta layer in all measurements for the same reason and also because of another source of artifacts: the Pt $M_{4,5}$ edge at 2200 eV overlaps with a minor Ta edge (the Ta M_2), which lies within the energy integration window used here for Pt [see Fig. 4(a)]. Thus, the Pt signal does not appear to drop to zero well within the Ta layer, as an unavoidable artefact of the integration procedure.

Nevertheless, the Co layer can clearly be detected between the Pt and Ta oxide layers, with an approximate thickness of 1 nm (measured as the approximate full width at half-maximum of the Co signal peak), consistent with the nominal value and the fitting of the reflectometry data [Fig. 1(c)]. The order of the profiles, from top to bottom, matches the data in panel (a): the upper set represents the initial measurement at room temperature, while from top to bottom the rest of the panels represent increasing temperatures down to the final quench to return to RT. The Gr layer should be in between the Co and the Ta layers, and it is not expected to suffer major changes or to affect the Co/Pt interface, since the temperature range studied here is in the order of the values that can be used for Co intercalation.

No significant changes are observed in either the Pt or Co profiles in Fig. 4(b) while heating up to 473 K. This behavior is expected as the intercalation temperature for Gr/Co/Pt(111) heterostructures under UHV conditions is below ∼600 K [18]. However, around 523 K, the center of mass of the Co elemental signal peak starts to shift into the Pt layer, drifting away from the Pt /Ta signals crossover point. This trend continues to increase at higher temperatures, with the largest displacement observed at the final linescan at 773 K, where the Co profile has completely shifted into the Pt layer so that the Pt and Co profiles completely overlap. After quenching back to RT, the complete Co signal, i.e., the whole thickness of the Co layer, stays located in the Pt layer, well below the crossover point of Pt and Ta signals. Simultaneously, the Pt signal has slightly dropped from previous values near the Pt /Ta crossover point. These findings hint that Co atoms may have completely moved into the Pt layer, giving rise to a Co-Pt alloy, as a consequence of the thermally activated process.

The chemical relative composition can be quantified from the EELS signals using the standard routine available in the software *Gatan Digital Micrograph*, which takes into account

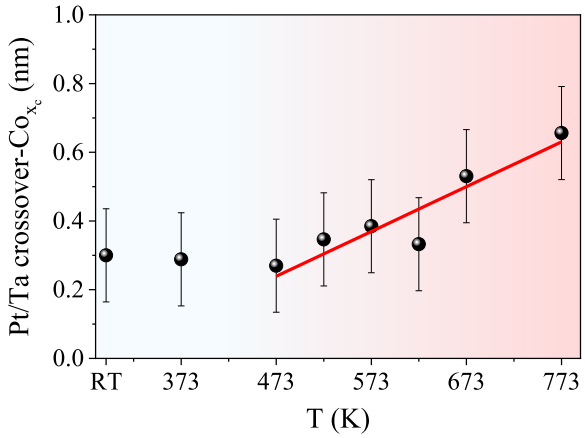

FIG. 5. Net distance from the middle of the Co layer (x_c) to the Pt/Ta signals crossover point as a function of annealing temperature, showing how the Co layer center of mass is drifting into the Pt layer after being annealed at temperatures above 473 K. Error bars are obtained from the Gaussian fit.

the scattering cross sections. Figure 4(c) shows the Co (blue), Pt (red), and Ta (black) relative compositions in at. %, calculated for all scans in panel (a1–a9), on a matching vertical scale. We must comment on two artifacts before extracting any conclusion from this graph. First, and because of the significant overlap in energy of the Pt/Ta edges, an accurate measurement of the Pt/Ta ratio is not possible for locations within the Ta layer. Nevertheless, this issue does not significantly affect the quantification of the Co/Pt atomic ratio. Also, since the Co layer is very thin (and the tails of the Pt and Ta EELS signals are noticeable in the region of the Co layer), the net Co content in the middle of the ultrathin Co layer never reached values of 100%, but this is to be expected considering electron beam broadening occurring due to channeling as already discussed. Despite this artifact, the position of the Co layer can be accurately quantified using a Gaussian fit to the data, as we will discuss next.

In fact, the presence of thermally activated diffusion processes above 523 K that give rise to Co-Pt alloying can be

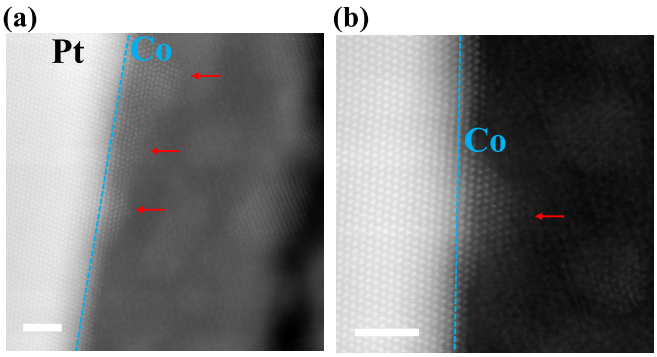

FIG. 6. HAADF-STEM atomic resolution images of the Gr/Co/Pt(111) interface at (a) 623 K and (b) 673 K after the EELS linescans were acquired. Red arrows indicate the areas where the electron beam had been positioned while the EELS data were acquired, and small Co islands appear giving the aspect of a locally rough islandlike growth. Scale bars correspond to 2 nm.

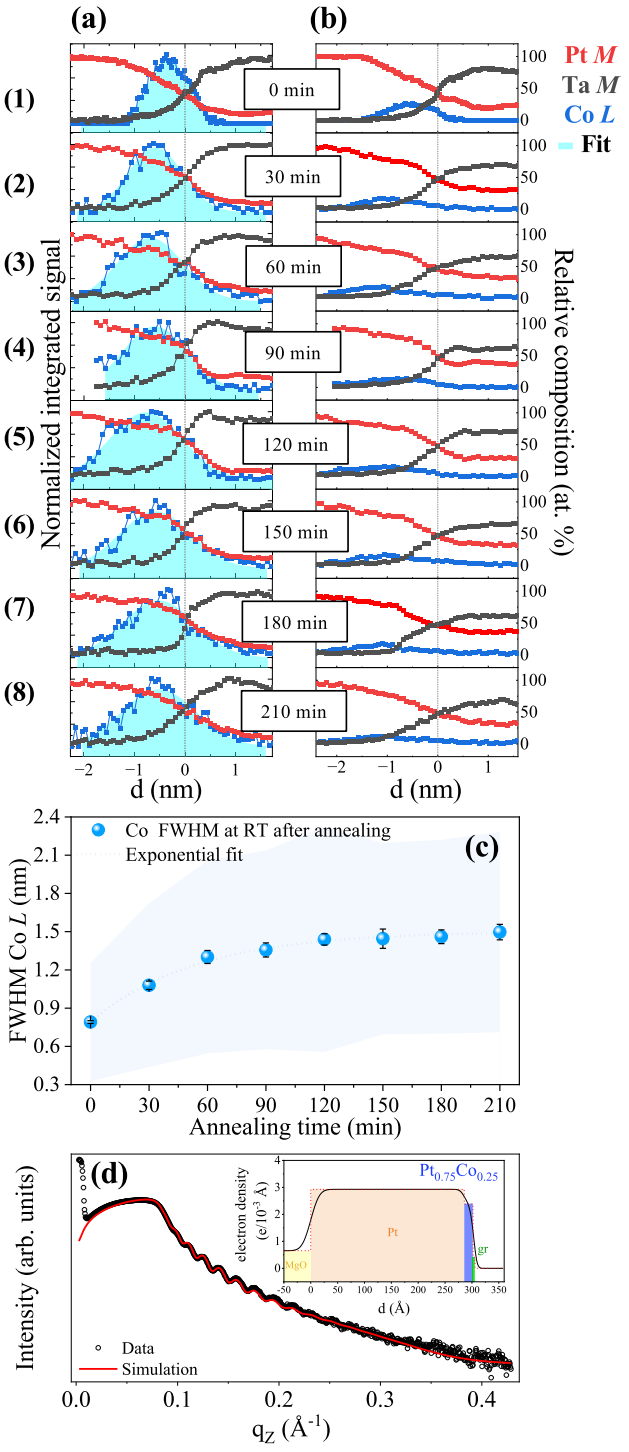

FIG. 7. (a) Normalized integrated signals extracted from the Co (blue), Pt (red), and Ta (black) edges across the Ta/Gr/Co/Pt(111) stack after sequential annealing intervals at 773 K. The data were extracted from EELS linescans (not shown) measured at RT after annealing times of 0, 30, 60, 90, 120, 150, 180, and 210 min, respectively, from top to bottom. Gaussian fits to the Co signal profiles are shown in solid cyan. (b) Relative composition, in atomic percent, for Co (blue), Pt (red), and Ta (black) species, calculated for all linescans on a matching order from top to bottom. (c) Width of the Co layer at RT after annealing the sample at 773 K, estimated as the FWHM of the Gaussian fit to the Co signal line profiles. Error bars are obtained from the Gaussian fit. A light blue band exhibits a value of 50% of the FWHM parameter itself. (d) XRR measurement (data points) and data simulation (solid red line) from an *ex situ* annealed Gr/Co(1)/Pt(30) stack deposited on MgO[111]. The inset shows the electron density profile of the simulated model used as a function of depth within the heterostructure. Different blocks corresponding to the substrate (MgO), $Pt_{75}Co_{25}$, and graphene (gr) layers have been highlighted in yellow, orange, blue, and green, respectively.

deduced from the quantification of the line profiles. The data do not allow us to extract accurately the precise onset for thermal activation, so we will take this value as an approximate estimation. The Co $L_{2,3}$ edge integrated signal [Fig. 4(b)] has been fitted as a normal distribution (solid cyan background) in order to quantify the position and layer width. Figure 5 depicts the absolute value of the distance from the center of this Gaussian fit (x_c) to the intersection point of the Pt and Ta signals, which has been used as the reference origin (zero value) for the spatial coordinate. While the center of the Co layer remains at a distance of 0.2–0.3 nm (around 1 atomic ML) up to annealing temperatures of 473 K—as one would expect since the Co layer is 3 ML thick—a steadily increasing shift into the Pt layer (marked with a red solid line, for clarity) is observed when the temperature increases above 523 K. This behavior results from a steady drift of Co species into the Pt layer when T increases, as a result of Co-Pt alloying.

The Co layer thickness could, in principle, be extracted as well from the Gaussian fits as the full width at half-maximum (FWHM), and one would expect for it to increase if chemical alloying is taking place. We must, however, comment on an interesting effect that impedes such direct quantification of accurate layer widths from the analysis of EEL linescans acquired *in situ* while the sample is hot. While slowly scanning the electron beam at high temperatures (approximately > 600 K) across the Co layer, the thin Co layer undergoes electron-beam-induced recrystallization processes likely associated with the thermally activated diffusion of Co atoms itself. Figure 6 depicts atomic resolution HAADF images obtained at 623 K (a) and 673 K (b) right after EELS acquisition. The Pt buffer retains its epitaxial and coherent structure, as expected since the conventional growth of graphene through CVD typically involves heating the Pt buffer to temperatures exceeding 973 K, following quenching to RT. However, nanometric Co islands appear near the regions where the electron beam was scanned that were not present before, marked with red arrows in Fig. 6. Such recrystallization processes at high temperatures have been reported before, as we will discuss later. They may affect a quantitative estimation of the Co layer width based on the FWHM of the Gaussian fit resulting from a local EELS measurement at high temperatures. Still, the data presented so far show that the onset interdiffusion processes take place at temperatures above 523 K, approximately, with full activation at temperatures above 673 K.

Therefore, and in order to accurately measure changes in Co layer thicknesses due to thermally induced interdiffusion mechanisms, we must avoid artifacts derived from beam-induced recrystallization. For this aim, we resorted to EELS acquisition at RT. Sequential annealing processes at 773 K were conducted for longer and longer time intervals. In be-

TABLE I. Parameters obtained from the exponential growth fit depicted in Fig. 7(c) marked with a blue dashed line.

Equation	y_0 (nm)	A (nm)	R_0 (min^{-1})
$y = y_0 - A\, e^{-R_0 t}$	1.496 $\pm$ 0.016	0.707 $\pm$ 0.019	0.0191 $\pm$ 0.0015

tween such intervals, the sample was quenched to RT and stabilized for 30 min. Then EELS linescans were acquired at RT before warming up again to 773 K for further specimen annealing. Figure 7(a) depicts the normalized integrated EEL signals extracted from EELS linescans as the annealing time increased. Again, signals shown correspond to the Co $L_{2,3}$ (blue), Pt $M_{4,5}$ (red), and Ta $M_{4,5}$ (black) edges as a function of distance across the scan. Figure 7(b) depicts the chemical relative composition from the EELS, on a matching vertical scale. Again, Gaussian fits (in cyan) were used to extract quantitative data from the Co signal profiles. Since RT measurements do not exhibit any major artifacts related to recrystallization, we could successfully extract meaningful values for the evolution of Co layer thickness with annealing time from the FWHM of the ensuing Gaussian fits to the Co $L_{2,3}$ normalized integrated intensity profiles.

Figure 7(c) presents the FWHM of the fits to the Co $L_{2,3}$ signal in (a) as a function of a total annealing time at 773 K. The error bars shown are those derived from the Gaussian fit. A light blue band has been added to reflect 50% of the actual value of the FWHM itself in order to account for the possibility of larger sources of uncertainty, such as any remaining electron-beam-induced effects. As annealing time increases, the Co layer progressively broadens, indicating enhanced diffusion into the Pt layer. The Co layer width increases fast, with values doubling from 0.7 to 1.5 nm, up to a total annealing time of 120 min, and then it reaches a plateau near 1.5 nm for higher times, possibly indicating that the equilibrium Co-Pt composition has been reached for that temperature. This behavior can be fitted to an exponential growth function (dashed blue line, for visual purposes) of the type $y = y_0 - A\ e^{-R_0 t}$, where R_0 would be the inverse characteristic time constant, and $(y_0 - A)$ would represent the initial value of the Co layer width. Table I summarizes the values of the parameters obtained from the data fitting.

To check whether these local changes measured by *in situ* STEM-EELS would be consistent with macroscopically averaged trends induced by a similar annealing, a similar Gr/Co(1 nm)/Pt(30 nm)/MgO[111] heterostructure was annealed *ex situ* at 773 K under vacuum (4×10^{-8} mbar) for 90 min in order to mimic the *in situ* experiments. Figure 7(d) exhibits the resulting XRR measurement (black datapoints) along with the fitting (red line) and electron density profiles (inset). In this case, the experimental data were simulated by substituting the Co layer for a $Pt_{0.75}Co_{0.25}$ alloy layer (density = 17.3429 g/cm^3). The fitting shows that the *ex situ* annealing results in a slight reduction of the Pt layer thickness from 30.0 to 28.6 nm, while a layer of $Pt_{0.75}Co_{0.25}$ alloy 1.6 nm thick is detected. The roughness of the Pt interface is reduced after the annealing by 50%, going from 1.4 to 0.7 nm. Meanwhile, the roughness at the graphene interface is maintained at 0.5 nm. These findings are fully consistent with the local *in situ* STEM-EELS findings.

IV. DISCUSSION

Our measurements show how Co-Pt interfacial alloying takes place as a result of thermally activated interdiffusion of Co into Pt. When heating at 523 K, a shoulder appears in the Pt signal tail at the Co-Pt interface in Fig. 4(c), marking the onset of the Co-Pt intermixing process as the Co species drift into the Pt layer. This shoulder exhibits approximately the same width as the Co layer, as one would expect from substitutional alloying. The Pt relative atomic composition near the Co/Pt interface, which was 100% at approximately 1 nm from the Pt/Ta signals crossover at RT, smoothly decreases as the annealing proceeds and Co intermixing increases. This decrease becomes particularly evident after the postannealing quenching [bottom panel of Fig. 4(c)], with a 100% Pt signal barely attained over 2 nm away from the Pt/Ta signals crossover. In the end, our estimation is that a Co-Pt intermixed layer appears, with an approximate thickness of 2 nm and an approximate chemical composition near $Pt_{75}Co_{25}$, although a precise number is hard to ascertain due to the aforementioned beam broadening effects along with the significant Ta signal tail into the alloyed Co-Pt layer. Nevertheless, these intermixing processes should, indeed, explain the changes in the magnetic properties highlighted in Fig. 2.

While our observations are consistent with the previous XPS studies, it is worth noting that the temperature ranges in which changes are found in this study are lower than those previously reported, which took place at temperatures of 595 K and above. Both ambient pressure and heating dynamics are likely contributors to the slightly lower intermixing temperature observed here ($\sim$523 K). We ascribe such differences to factors such as standard vacuum conditions of the STEM microscope column, around 10^{-6} to 10^{-5} Pa, while XPS reports were conducted under UHV conditions ($\sim 10^{-9}$ Pa). This pressure difference suggests that the temperatures at which intermixing begins may depend on ambient pressure, which may affect kinetic interactions among atoms or molecules, potentially leading to a lower observed intermixing temperature under standard vacuum conditions in much thinner specimens. In addition to pressure, the rate of temperature increase, faster thermalization of thin TEM specimens, or timing of measurements are also relevant factors. The local character of STEM-EELS measurements should also be taken into account when comparing both types of data. For example, the electron beam may also contribute to a slight local heating of the samples by a few tens of degrees, or it could supply energy to the sample via other mechanisms, as we will discuss next.

In fact, artifacts derived from the interaction of the electron beam with the sample are also relevant during STEM measurements with atomic size electron probes. At high enough temperatures, the beam-sample interaction may trigger specific atomistic diffusion mechanisms. As the electron beam is slowly scanned across the Co layer on the hot sample, thermally activated local recrystallization processes may give rise to nucleation of nanocrystals, as shown in Fig. 6. Electron-beam-induced nucleation of coherent Co islands at high temperatures (>623 K) promotes a local thickening of

the Co layer within a lateral island size in the nm range. Similar effects have been observed before, e.g., as previously reported by Jesse *et al.* [27], where e-beam raster scanning resulted in the recrystallization of ion-beam-amorphized STO grown on an STO single crystal, transforming it into an epitaxial STO crystal lattice. Typically, sample damage or modification by an incident electron beam can be attributed to two primary mechanisms: first, the ballistic interaction of the fast electron with an atomic nucleus, causing atomic displacement (knock-on damage); second, the excitation of an atomic electron beyond the Fermi level, which temporarily leaves a hole that may destabilize the atomic bonding, leading to structural changes (radiolysis) [28]. While an in-depth explanation of these processes is beyond the scope of this paper, we could wonder whether radiolysis plays a significant role in our observations. This phenomenon has also been discussed, particularly in annealed samples, as atomic-scale reconstructions at oxide interfaces [29]. However, in our case these features tend to disappear over time as the electron beam is placed somewhere else if the temperature stays high, so the Co layer is locally annealed back to a smooth, flat state. Thus, we believe that the Co atoms rearrange without any material loss (sputtering), so we suggest that our Co surface recrystallization is more likely attributable to knock-on damage. Still, the Co diffusion processes towards the Pt layer remain active, as shown by the shift depicted in Fig. 5.

V. CONCLUSIONS

In summary, here we show a high-resolution STEM-EELS *in situ* study of thermally driven intermixing processes at Co/Pt interfaces within Gr/Co/Pt(111) heterostructures. Our results indicate that significant Co/Pt interfacial interdiffusion mechanisms become active around temperatures of 523 K and above, with full intermixing occurring after annealing times of tens of minutes above 673 K. In fact, annealing processes approximately 60 min long at 773 K already lead to an equilibrium configuration consisting of a fully intermixed 1.5-nm-thick layer of a $Pt_{75}Co_{25}$ alloy in our case. The magnetic properties of such intermixed Co/Pt layers change significantly upon alloying, with enhanced coercivities probably due to an increased PMA. The exponential progression of this intermixing highlights the importance of precise temperature control during growth or other procedures such as Co intercalation in heterostructures. Such processes could also become relevant during operation of devices based on such systems if the magnetic properties were to be optimized for spintronic applications. In fact, our data also provide a range of operating temperatures for devices based on these multilayers, which should lie in the <523 K temperature range. These findings improve our understanding of the structural and magnetic interactions in these heterostructures, and they pave the way for more accurate engineering of Gr-based spin-electronic devices, which are set to change future sensing and data storage technologies, as well as Boolean and non-Boolean computation.

ACKNOWLEDGMENTS

Electron microscopy observations were carried out at the Centro Nacional de Microscopía Electrónica at UCM (ICTS ELECMI - Madrid). Preparation by FIB was carried out at the Laboratorio de Microscopías Avanzadas (ICTS ELECMI–Zaragoza). Financial support from the Spanish Ministry for Science [Grants No. PID2021-122980OB-C51, No. PID2021-122980OB-C52 (ECLIPSE), No. PID2020-117024GB-C43, and No. CNS2022-136143 (SPINCODE)] and Comunidad de Madrid [Grants No. TEC-2024/TEC-380 (Mag4TIC-CM), No. MAD2D-CM-UCM3, and No. MAD2D-CM-UAM] is acknowledged. A.G-M. acknowledges support from MINECO through Grant No. RTI2018-097895-B-C43. F.A. acknowledges Comunidad de Madrid Atracción de Talento program (2022-T1/IND-23901).

DATA AVAILABILITY

The data that support the findings of this article are not publicly available. The data are available from the authors upon reasonable request.

[1] S. D. Bader and S. S. P. Parkin, Spintronics, Annu. Rev. Condens. Matter Phys. **1**, 71 (2010).

[2] I. Žutić, J. Fabian, and S. Das Sarma, Spintronics: Fundamentals and applications, Rev. Mod. Phys. **76**, 323 (2004).

[3] A. Soumyanarayanan, N. Reyren, A. Fert, and C. Panagopoulos, Emergent phenomena induced by spin-orbit coupling at surfaces and interfaces, Nature (London) **539**, 509 (2016).

[4] J. C. Rojas-Sánchez and A. Fert, Compared efficiencies of conversions between charge and spin current by spin-orbit interactions in two- and three-dimensional systems, Phys. Rev. Appl. **11**, 054049 (2019).

[5] A. Anadón, A. Pezo, I. Arnay, R. Guerrero, A. Gudín, A. Guio, M. Yactayo, J. Ghanbaja, J. Camarero, A. Manchon, S. Petit-Watelot, and P. Perna, J.-C. Rojas-Sánchez, Giant and anisotropic enhancement of spin-charge conversion in graphene-based quantum system, Adv. Mater. **37**, 2418541 (2025).

[6] M. Piquemal-Banci, R. Galceran, S. M.-M. Dubois, V. Zatko, M. Galbiati, F. Godel, M.-B. Martin, R. S. Weatherup, F. Petroff, A. Fert, Spin filtering by proximity effects at hybridized interfaces in spin-valves with 2D graphene barriers, Nat. Commun. **11**, 5670 (2020).

[7] S. Lancaster, I. Arnay, R. Guerrero, A. Gudín, A. Guedeja-Marrón, J. M. Diez, J. Gärtner, A. Anadón, M. Varela, J. Camarero, T. Mikolajick, P. Perna, and S. Slesazeck, Toward nonvolatile spin–orbit devices: Deposition of ferroelectric hafnia on monolayer graphene/Co/HM stacks, ACS Appl. Mater. Interfaces **15**, 16963 (2023).

[8] M. Jugovac, I. Cojocariu, J. Sánchez-Barriga, P. Gargiani, M. Valvidares, V. Feyer, S. Blügel, G. Bihlmayer, and P. Perna, Inducing single spin-polarized flat bands in monolayer graphene, Adv. Mater. **35**, 2301441 (2023).

[9] A. Anadón, A. Gudín, R. Guerrero, I. Arnay, A. Guedeja-Marron, P. Jiménez-Cavero, J. M. D. Toledano, F. Ajejas,

M. Varela, S. Petit-Watelot *et al.*, Engineering the spin conversion in graphene monolayer epitaxial structures, APL Mater. **9**, 061113 (2021).

[10] A. Gudín, A. Anadón, I. Arnay, R. Guerrero, J. Camarero, S. Petit-Watelot, P. Perna, and J.-C. Rojas-Sánchez, Isotropic spin and inverse spin Hall effect in epitaxial (111)-oriented Pt/Co bilayers, Phys. Rev. Mater. **7**, 124412 (2023).

[11] E. Díaz, A. Anadón, P. Olleros-Rodríguez, H. Singh, H. Damas, P. Perna, M. Morassi, A. Lemaître, M. Hehn, and J. Gorchon, Energy-efficient picosecond spin–orbit torque magnetization switching in ferro- and ferrimagnetic films, Nat. Nanotechnol. **20**, 36 (2025).

[12] V. M. Karpan, G. Giovannetti, P. A. Khomyakov, M. Talanana, A. A. Starikov, M. Zwierzycki, J. van den Brink, G. Brocks, and P. J. Kelly, Graphite and graphene as perfect spin filters, Phys. Rev. Lett. **99**, 176602 (2007).

[13] F. Calleja, H. Ochoa, M. Garnica, S. Barja, J. J. Navarro, A. Black, M. M. Otrokov, E. V. Chulkov, A. Arnau, A. L. V. de Parga, F. Guinea, and R. Miranda, Spatial variation of a giant spin–orbit effect induces electron confinement in graphene on Pb islands, Nat. Phys. **11**, 43 (2015).

[14] F. Ajejas, A. Gudín, R. Guerrero, A. A. Barcelona, J. M. Diez, L. de M. Costa, P. Olleros, M. A. Niño, S. Pizzini, J. Vogel *et al.*, Unraveling Dzyaloshinskii–Moriya interaction and chiral nature of graphene/cobalt interface, Nano Lett. **18**, 5364 (2018).

[15] M. Blanco-Rey, P. Perna, A. Gudín, J. M. Diez, A. Anadón, P. Olleros-Rodrguez, L. de M. Costa, M. Valvidares, P. Gargiani, A. Guedeja-Marron *et al.*, Large perpendicular magnetic anisotropy in nanometer-thick epitaxial graphene/co/heavy metal heterostructures for spin–orbitronics devices, ACS Appl Nano Mater **4**, 4398 (2021).

[16] B. Muñiz Cano, A. Gudín, J. Sánchez-Barriga, O. Clark, A. Anadón, J. M. Díez, P. Olleros-Rodríguez, F. Ajejas, I. Arnay, M. Jugovac *et al.*, Rashba-like spin textures in graphene promoted by ferromagnet-mediated electronic hybridization with a heavy metal, ACS Nano **18**, 15716 (2024).

[17] M. Varela, A. R. Lupini, K. van Benthem, A. Y. Borisevich, M. F. Chisholm, N. Shibata, E. Abe, and S. J. Pennycook, Materials characterization in the aberration-corrected scanning transmission electron microscope, Annu. Rev. Mater. Res. **35**, 539 (2005).

[18] F. Ajejas, A. Anadon, A. Gudin, J. M. Diez, C. G. Ayani, P. Olleros-Rodríguez, L. de M. Costa, C. Navío, A. Gutierrez, F. Calleja *et al.*, Thermally activated processes for ferromagnet intercalation in graphene-heavy metal interfaces, ACS Appl. Mater. Interfaces **12**, 4088 (2020).

[19] S. Lichtert and J. Verbeeck, Statistical consequences of applying a PCA noise filter on EELS spectrum images, Ultramicroscopy **125**, 35 (2013).

[20] G. Vignaud and A. Gibaud, *REFLEX*: A program for the analysis of specular X-ray and neutron reflectivity data, J. Appl. Crystallogr. **52**, 201 (2019).

[21] P. Perna, C. Rodrigo, E. Jiménez, F. J. Teran, N. Mikuszeit, L. Méchin, J. Camarero, and R. Miranda, Tailoring magnetic anisotropy in epitaxial half metallic $La_{0.7}Sr_{0.3}MnO_3$ thin films, J. Appl. Phys. **110**, 013919 (2011).

[22] P. Perna, D. Maccariello, F. Ajejas, R. Guerrero, L. Méchin, S. Flament, J. Santamaria, R. Miranda, and J. Camarero, Engineering large anisotropic magnetoresistance in $La_{0.7}$ $Sr_{0.3}$ MnO_3 films at room temperature, Adv. Funct. Mater. **27**, 1700664 (2017).

[23] C. C. Ahn and O. L. Krivanek, *EELS Atlas: A Reference Guide of Electron Energy Loss Spectra Covering All Stable Elements* (Gatan, Warrendale, PA, 1983).

[24] S. Vijayan, R. Wang, Z. Kong, and J. R. Jinschek, Quantification of extreme thermal gradients during in situ transmission electron microscope heating experiments, Microsc. Res. Tech. **85**, 1527 (2022).

[25] T. P. van Swieten, T. van Omme, D. J. van den Heuvel, S. J. W. Vonk, R. G. Spruit, F. Meirer, H. H. P. Garza, B. M. Weckhuysen, A. Meijerink, F. T. Rabouw, and R. G. Geitenbeek, Mapping elevated temperatures with a micrometer resolution using the luminescence of chemically stable upconversion nanoparticles, ACS Appl. Nano Mater. **4**, 4208 (2021).

[26] T. Malis, S. C. Cheng, and R. F. Egerton, EELS log-ratio technique for specimen-thickness measurement in the TEM, J. Electron Microsc. Tech. **8**, 193 (1988).

[27] S. Jesse, Q. He, A. R. Lupini, D. N. Leonard, M. P. Oxley, O. Ovchinnikov, R. R. Unocic, A. Tselev, M. Fuentes-Cabrera, B. G. Sumpter, S. J. Pennycook, S. V. Kalinin, and A. Y. Borisevich, Atomic-level sculpting of crystalline oxides: Toward bulk nanofabrication with single atomic plane precision, Small **11**, 5895 (2015).

[28] R. F. Egerton, Radiation damage to organic and inorganic specimens in the TEM, Micron **119**, 72 (2019).

[29] G. Segantini, C.-Y. Hsu, C. W. Rischau, P. Blah, M. Matthiesen, S. Gariglio, J.-M. Triscone, D. T. L. Alexander, and A. D. Caviglia, Electron-beam writing of atomic-scale reconstructions at oxide interfaces, Nano Lett. **24**, 14191 (2024).